Research Article

Deep-tissue two-photon microscopy with a frequency-doubled all-fiber mode-locked laser at 937 nm

Hongsen He,[a,†] Huajun Tang,[a,†] Meng Zhou,[a] Hei Ming Lai,[b,c,d] Tian Qiao,[a,*] Yu-xuan Ren,[e] Cora S. W. Lai,[f,g] Ho Ko,[b,c,d] Xiaoming Wei,[h] Zhongmin Yang,[h] Kevin K. Tsia,[a,i] and Kenneth K. Y. Wong [a,i,*]

[a]University of Hong Kong, Department of Electrical and Electronic Engineering, Hong Kong, China
[b]Chinese University of Hong Kong, Faculty of Medicine, Department of Psychiatry, Hong Kong, China
[c]Chinese University of Hong Kong, Faculty of Medicine, Department of Medicine and Therapeutics, Hong Kong, China
[d]Chinese University of Hong Kong, Prince of Wales Hospital, Li Ka Shing Institute of Health Sciences, Hong Kong, China
[e]Fudan University, Shanghai Medical College, Institute for Translational Brain Research, Shanghai, China
[f]University of Hong Kong, School of Biomedical Sciences, Li Ka Shing Faculty of Medicine, Hong Kong, China
[g]University of Hong Kong, State Key Laboratory of Brain and Cognitive Sciences, Hong Kong, China
[h]South China University of Technology, School of Physics and Optoelectronics, Guangzhou, China
[i]Advanced Biomedical Instrumentation Centre, Hong Kong, China

Abstract. In two-photon microscopy, low illumination powers on samples and a high signal-to-noise ratio (SNR) of the excitation laser are highly desired for alleviating the problems of photobleaching and phototoxicity, as well as providing clean backgrounds for images. However, the high-repetition-rate Ti: sapphire laser and the low-SNR Raman-shift lasers fall short of meeting these demands, especially when used for deep penetrations. Here, we demonstrate a 937-nm laser frequency-doubled from an all-fiber mode-locked laser at 1.8 μm with a low repetition rate of ~9 MHz and a high SNR of 74 dB. We showcase two-photon excitations with low illumination powers on multiple types of biological tissues, including fluorescence imaging of mouse brain neurons labeled with green and yellow fluorescence proteins (GFP and YFP), DiI-stained and GFP-labeled blood vessels, Alexa Fluor 488/568-stained mouse kidney, and second-harmonic-generation imaging of the mouse skull, leg, and tail. We achieve a penetration depth in mouse brain tissues up to 620 μm with an illumination power as low as ~10 mW, and, even for the DiI dye with an extremely low excitation efficiency of 3.3%, the penetration depth is still up to 530 μm, indicating that the low-repetition-rate source works efficiently for a wide range of dyes with a fixed excitation wavelength. The low-repetition-rate and high-SNR excitation source holds great potential for biological investigations, such as *in vivo* deep-tissue imaging.

Keywords: 1.8 μm laser; low repetition rate; high signal-to-noise ratio; mouse brain; fluorescence and second-harmonic-generation imaging.

Received May 19, 2022; revised manuscript received Jul. 5, 2022; accepted for publication Jul. 22, 2022; published online Aug. 11, 2022.

1 Introduction

Two-photon microscopy (2PM) has been a reliable and efficient tool for noninvasive deep-tissue imaging in biomedical investigations.[1–4] It offers multiple advantages, including deeper tissue penetration, optical sectioning without a need for pin-holes, and less photodamage compared with confocal micros-copy. Remarkably, within the past few years, high-speed innovations have been applied in the 2PM, realizing kilohertz frame rate.[2] The performance of 2PM is largely determined by the properties of the excitation laser, including wavelength, peak power, and repetition rate.[5] While a high power is

*Address all correspondence to Tian Qiao, qtjoansherry@gmail.com; Kenneth K. Y. Wong, kywong@eee.hku.hk

†These authors contributed equally to this work.

beneficial for achieving high-brightness two-photon images, excessive light exposure leads to photobleaching and photo-damage—one of the most significant challenges to overcome in 2PM.[6,7] An alternative and more efficient strategy is to build an excitation laser with a low repetition rate, which has been shown to provide more efficient excitation given the same average power.[8] Since repetition rate is usually determined by the length of the laser cavity, solid-state lasers, such as the Ti:sapphire mode-locked laser, are not suitable for outputting low-repetition-rate signals, as a few meters long optical path of the oscillator in the free space is clearly impracticable in most applications. In contrast, an all-fiber laser can be mode-locked at a low repetition rate by conveniently adding a few dozen meters of fibers in the oscillator, resulting in a space-saving system.

The wavelengths used for two-photon excitation of fluorophores tend to be in the infrared spectrum between 800 and 1000 nm, among which ∼930 nm is one of the most popular wavelengths used for imaging green fluorescent protein (GFP) and its mutants.[9–12] In recent years, the realizations of ∼930 nm fiber lasers can be classified into two groups. The first group directly mode-locks lasers at the ∼930-nm region using neodymium (Nd) doped fiber.[9,10] A major limitation of Nd doped fiber is the lower gain of the desired three-level transition than its standard four-level transition, thus low temperature,[13] phosphate glasses,[14] co-doped gain fibers,[15] or specified fiber structures[16–18] are required to enhance the process. Furthermore, the power amplification of the ∼930-nm laser is also complex and relatively difficult based on the above methods, as the four-level transition also needs to be suppressed in the amplifiers to avoid the amplified spontaneous emission (ASE) at ∼1080 nm. The other popular technique is to utilize nonlinear frequency conversion, such as shifting a 1-μm laser to the 930-nm region[19,20] or Raman shifting a 1.5-μm laser to the 1.8-μm region,[11,12,21–24] followed by frequency doubling. Photonic crystal rods/fibers (PCF)[19–21] or large-mode-area fibers[11,23,24] are generally employed to provide required nonlinearities, which usually hinder an all-fiber configuration. Besides, an energetic 1.5-μm source is necessary to excite the nonlinearities, and the desired wavelength usually occupies a small part of the output spectrum.[19,24] More importantly, the coherence of the newly generated frequency is usually degraded due to the enhanced noises during the frequency-shift process, especially using the PCF with very high nonlinearity,[25] which is detrimental for imaging quality. On the contrary, the direct mode-locked lasers always have the merit of offering a high signal-to-noise ratio (SNR).

In this work, we demonstrate a 937-nm laser frequency-doubled from an all-fiber mode-locked laser at 1.8 μm, with a low repetition rate of ∼9 MHz and a high SNR of 74 dB. Single-stage amplification is utilized to simultaneously boost the 1.8-μm power and compress the pulse width based on the self-phase-modulation (SPM) effect in the single-mode fiber (SMF). No optical filters or specialty fibers are needed in the laser system. We showcase two-photon excitations with the 937-nm laser on multiple biological tissue types, including imaging of GFP- and YFP-labeled mouse brain neurons, DiI-stained/GFP-labeled blood vessels, Alexa Fluor 488/568-stained mouse kidney, and second harmonic generation (SHG) imaging of the intact mouse skull, leg, and tail.
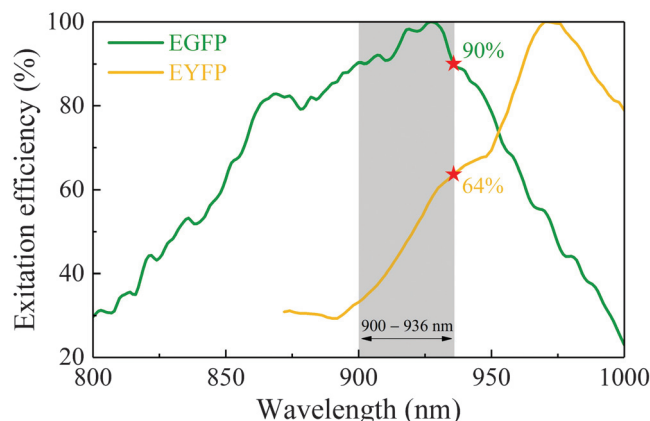
Fig. 1 Two-photon excitation efficiency of the EGFP and EYFP under the illumination from 800 to 1000 nm.

2 Excitation Wavelength Selection of the 2PM

Unlike Ti:sapphire lasers with wavelength tunability, fiber lasers usually output a fixed spectrum. In the multiphoton excitation regime, fluorophores typically have large excitation bandwidths, which allow fixed-wavelength lasers to excite a range of labels.[26,27] Thus, we aim to build an all-fiber mode-locked laser that can cover a few commonly used fluorophores. GFP and YFP are two widely used proteins in diverse neuroscience experiments and cellular assays. The two-photon excitation spectra of the enhanced GFP (EGFP) and enhanced YFP (EYFP)[28,29] are shown in Fig. 1. The excitation peak of the EGFP is located at 927 nm, and the excitation efficiency is over 90% from 900 to 936 nm, as shown in the gray shaded area. Within this wavelength window, the excitation efficiency of EYFP increases from 33% to 64%, which is nearly doubled. Therefore, we aim to develop a laser around 936 nm for versatile biological applications.

3 Experimental Configuration of the Excitation Laser

The configuration of the laser system is shown in Fig. 2(a), consisting of the laser oscillator, amplifier, and frequency-doubling parts. In the laser cavity, a semiconductor saturable absorber mirror (SESAM, SAM-1920-4-40ps-x, BATOP) was butt-coupled to the signal end of a 1570/1870-wavelength-division multiplexer (WDM-1) for achieving mode locking. A 6-cm-long thulium-doped fiber (TDF-1, TmDF200, OFS) was spliced between the common end of WDM-1 and one end of a 30/70 optical coupler (OC). The pump power was from a commercial 1570-nm laser. A nonlinear optical loop mirror (NOLM) was made by splicing two fiber branches on the other side of the OC to reflect the beam in the cavity. A polarization controller (PC) was put on the NOLM to provide an appropriate linear phase delay for pulses propagating in opposite directions. The fourth end of the OC served as the output of the laser oscillator. Apart from the TDF, other fibers used in the cavity were all SMFs (SMF-28e, Corning). The fiber lengths of the NOLM and linear part were about 1.4 and 10.5 m, respectively, which corresponded to a fundamental repetition rate of ∼8.9 MHz when the laser is mode locked. WDM-2 was spliced to the
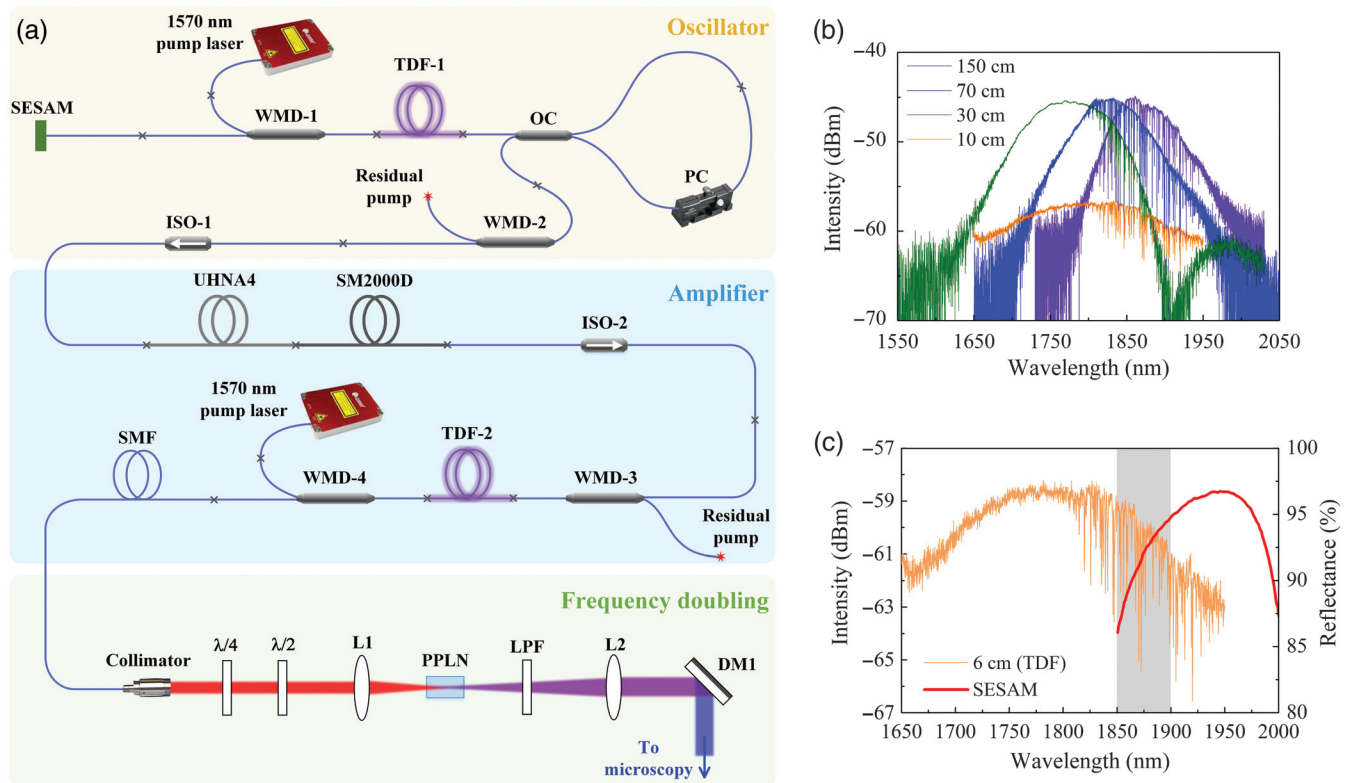
Fig. 2 (a) Experimental configuration of the all-fiber laser source and the frequency-doubling setup. (b) ASE spectra of the TDFs with different lengths (150, 70, 30, and 10 cm, respectively). (c) ASE spectrum of the 6-cm-long TDF and the reflectance of the SESAM as a function of the wavelength.

output of the laser oscillator for exporting the residual pump power. Two isolators (ISO-1 and ISO-2) were connected afterward to isolate the backward-propagation light from the optical amplifier to ensure the stability of the laser mode-locking in the oscillator. The group velocity dispersion (GVD) of the SMF is -0.066 ps^2/m at 1870 nm,[30] which provides anomalous dispersion.

Two bundles of normal dispersion fibers (NDF, 50-m UHNA4 and 48-m SM2000D, Coherent) were spliced between the two isolators to provide enough normal dispersion to stretch the laser pulses before the power boost. The GVDs of the UHNA4 and SM2000D fibers are 0.088 and 0.115 ps^2/m at 1870 nm,[30] respectively. The combination of UHNA4 and SM2000D enabled better compression results than a single fiber type owing to their opposite sign of third-order dispersion. The selection of the relative length of the two NDFs was mainly based on the final pulse shape to minimize the pedestal under the pulse. There were two main functions of the NDFs. First, the peak power of the chirped pulse after the NDFs remained relatively low to avoid strong nonlinearities at the initial stage of the power amplification.[31] The nonlinearity effect, such as the Raman shift, was not beneficial for the power amplification at the desired wavelength. Second, the SMFs in the amplifier provided the anomalous dispersion subsequently, which could compress the pulse, and, simultaneously, the increased peak power of the pulses was capable of stimulating the SPM effect during the power boosting, resulting in a broadened spectrum and further short laser pulses. The optical amplifier consisted of two WDMs (WDM-3 and WDM-4) and one piece of TDF-2

(14 cm, SM-TSF-5/125, Coherent). TDF-2 was backward pumped by the other 1570-nm laser through WDM-4, and the unabsorbed pump light was exported from the 1570-nm end of WDM-3. Around 6-m SMFs were used in the amplifier (equal to the total length of ISO-2, WDM-3, and WDM-4). Another 13-m SMF was spliced to the signal end of WDM-4 to optimize the SPM effect before the final output, realizing the shortest pulse width. The footprint of the all-fiber 1.8-μm source was around $30 \times 30 \times 5$ cm^3 with two layers to arrange the oscillator and amplifier, which was much more compact than the solid-state lasers and the fiber lasers using the optical filters and diffraction gratings. The layout of the fiber laser system is shown in Fig. S1 in the Supplemental Material. Furthermore, the fibers used in the 1.8-μm source were all telecommunication grade fibers, minimizing the cost for the laser establishment.

The amplified beam was then collimated by a fiber collimator to the free space. A 10-mm-long periodically poled lithium niobate (PPLN, CTL Photonics) crystal was used for frequency doubling to generate the signal at ~937 nm. The poling period of the PPLN crystal ranges from 17.3 to 28.9 μm. According to the quasiphase matching (QPM) condition, the QPM period for frequency-doubling the 1.8-μm laser is ~27.1 μm at room temperature, which is covered in this PPLN crystal. After finely tuning the lateral position of the focus spot around the desired QPM period and the temperature, the maximum efficiency can be achieved at 125°C. A half and a quarter waveplate were utilized to adjust the polarization direction of the 1.8-μm beam for maximizing the conversion efficiency of the SHG. The lenses L1 (focal length, $f_1 = 75$ mm) and L2 ($f_2 = 125$ mm) were used to

focus the 1.8-μm beam into the PPLN crystal and collimate the generated SHG signal, respectively. Three long-pass filters (Long Pass 633, 785, and 808, Semrock) and a dichroic mirror (DM, DMLP950, Thorlabs) were used aiming to clean up the signal of the fourth harmonic generation and the residual 1.8-μm beam, respectively, to make sure that only the 937-nm signal entered the microscopy.

4 Principle of Wavelength Selection and Laser Performance

The output wavelength of the laser oscillator was controlled by adjusting the TDF length rather than using the optical bandpass filters or gratings inside the laser cavity. Figure 2(b) demonstrates the ASE spectra of the TDF with different lengths. The center of the ASE spectrum is blueshifted when the TDF length is decreased from 150 to 30 cm, which is attributed to the shorter TDF having less self-absorption in the 1.7 to 1.8 μm region of the ASE. The ASE centers for the TDF lengths of 150, 70, and 30 cm are 1870, 1826, and 1775 nm, respectively. Notably, the

ASE center alone cannot determine the peak of the mode-locking wavelength, as the wavelength-dependent reflectance of the SESAM also plays an important role. The ASE peak shifts about 95 nm with the reduction of 120-cm TDF. The dip around 1910 nm of the 30-cm-TDF spectrum is owing to the frequency cutoff of the WDM. When the TDF length is further shortened to 10 cm, the ASE center is no more shifted to shorter wavelengths. The wavelength center is located at 1800 nm, while its ASE spectrum is much flatter than the 30-cm-TDF spectrum, resulting from both the low gain and low self-absorption of the relatively short TDF. To achieve the laser mode-locking at ~1.86 μm, we cut the TDF from a longer length. When reducing the TDF length in the laser oscillator, the mode-locked wavelength tends to be blueshifted. When the length of the TDF is shortened to 6 cm, the laser oscillator achieves a stable self-started mode-locking at ~1.86 μm under the pump power of 570 mW by tuning the PC. The mode-locking is realized by the balance between the gain and loss of the 1.86-μm signal circulating inside the laser cavity, which is mainly determined by the TDF emission and the reflectance of the SESAM, as shown
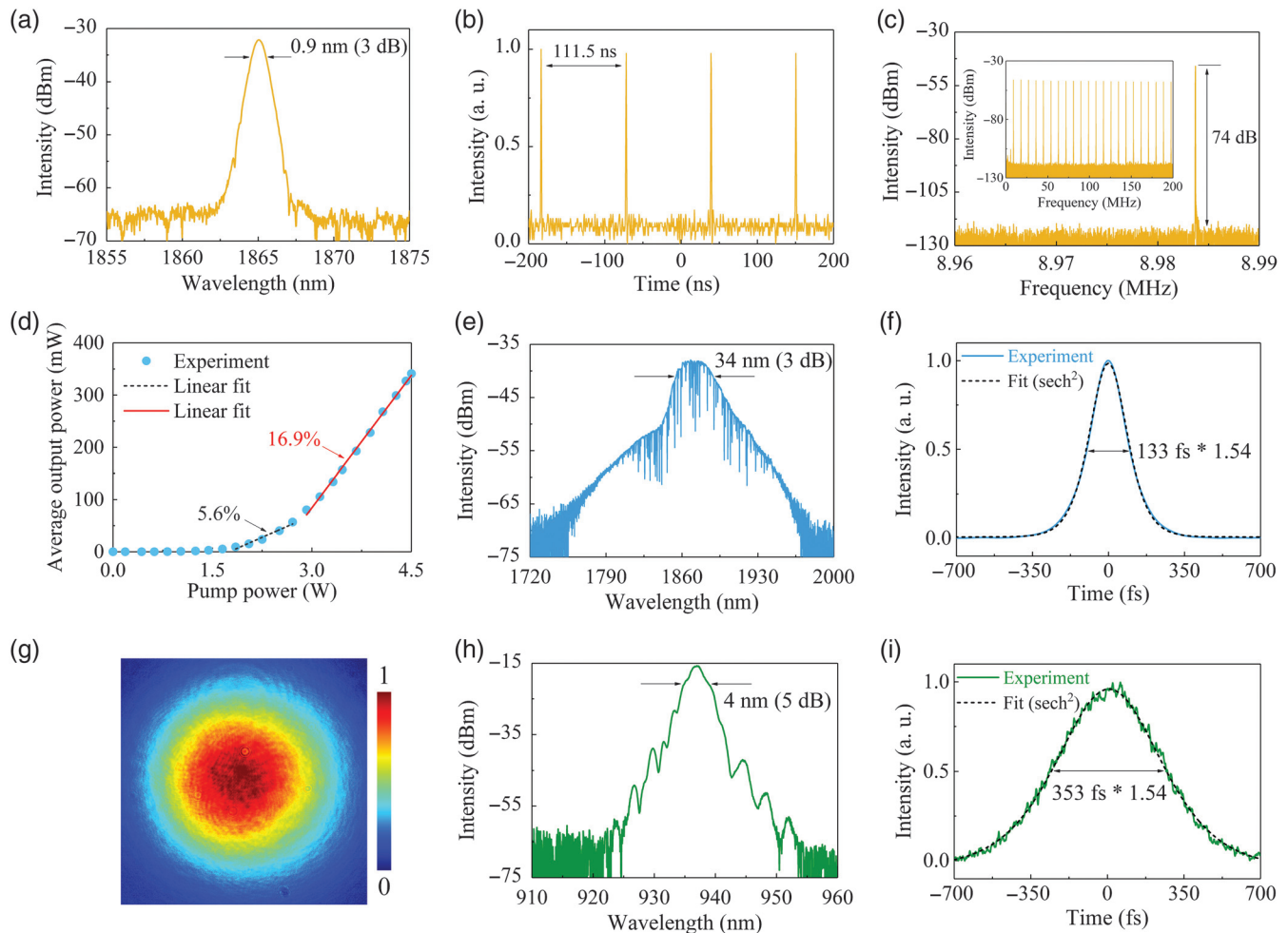
Fig. 3 (a) Spectrum of the laser oscillator in the mode-locked state. (b) Pulse train and (c) RF spectrum of the output signal from the laser oscillator. The inset of (c) is the RF spectrum within a 200-MHz span. (d) Average output power as a function of the pump power in the amplifier. (e) Spectrum and (f) pulse width of the amplified signal. (g) Beam profile of the frequency-doubled laser centered at 937 nm. (h) Spectrum and (i) pulse width of the frequency-doubled laser after the PPLN crystal. "a. u.": arbitrary units.

in Fig. 2(c). The ASE spectrum of the 6-cm TDF is similar to the 10-cm one. The SESAM reflectance increases from 86% to 95% in the wavelength region from 1850 to 1900 nm, while the ASE gain of the TDF has a 2-dB reduction, as indicated in the gray-shaded area of Fig. 2(c). Thus, a gain/loss balance can be achieved by the opposite effects from the SESAM and TDF, resulting in a stable mode-locked state inside the laser oscillator. The mechanism of the wavelength selection is merely based on the original elements in the laser cavity, making the laser system more compact and realizing an all-fiber scheme. This is also critical to maintaining the oscillator in a low-loss state, realizing self-started fundamental mode-locking instead of undesired high-order harmonic generations at the initial stage.[32] As extra wavelength-selecting elements inside the oscillator inevitably bring in more signal loss, this TDF-length-based method is more efficient for laser mode-locking below 1.9 μm, given the relatively low gain of the short TDF.

The wavelength peak of the mode-locked beam is at ~1865 nm, as shown in Fig. 3(a), measured by an optical spectrum analyzer (OSA, AQ6375, YOKOGAWA). The 3-dB bandwidth of the optical spectrum is 0.9 nm, which corresponds to a transform-limited $sech^2$ pulse width of 4 ps. The average output power was ~340 μW. The output pulse was detected by a fiber-coupled InGaAs photodetector (10 GHz, ET-5000F, EOT) and an oscilloscope (300 MHz, DS2302A, RIGOL). The pulse train demonstrates a 111.5-ns period, as shown in Fig. 3(b), corresponding to a repetition rate of ~9 MHz. The radio frequency (RF) spectrum was measured by an electrical spectrum analyzer (26 GHz, E4440A, Agilent). The SNR is ~74 dB, and the frequency peak is at 8.984 MHz, as shown in Fig. 3(c). A 200-MHz RF span illustrates a clean and flat spectrum, confirming the high SNR of the mode-locked laser. The pulse period and RF peak were consistent with the optical length of the laser cavity, confirming that the output laser operated at the fundamental mode-locking regime. The average output power as a function of the pump power in the amplifier is shown in Fig. 3(d). The output power begins to grow faster when the pump power is above 1.65 W. The slope efficiencies are 5.6% and 16.9% under the pump power of 1.65 to 2.7 and 2.7 to 4.5 W, respectively. Due to the heavily doped Tm^{3+}-ions in the TDF, the pump power had to be increased to ~1.65 W to observe a clear population inversion, while higher slope efficiency was observed when the pump power was above 2.7 W. The maximum output power is 341 mW obtained at a pump power of 4.5 W. During the power amplification stage, the SPM effect becomes dominant when the average output
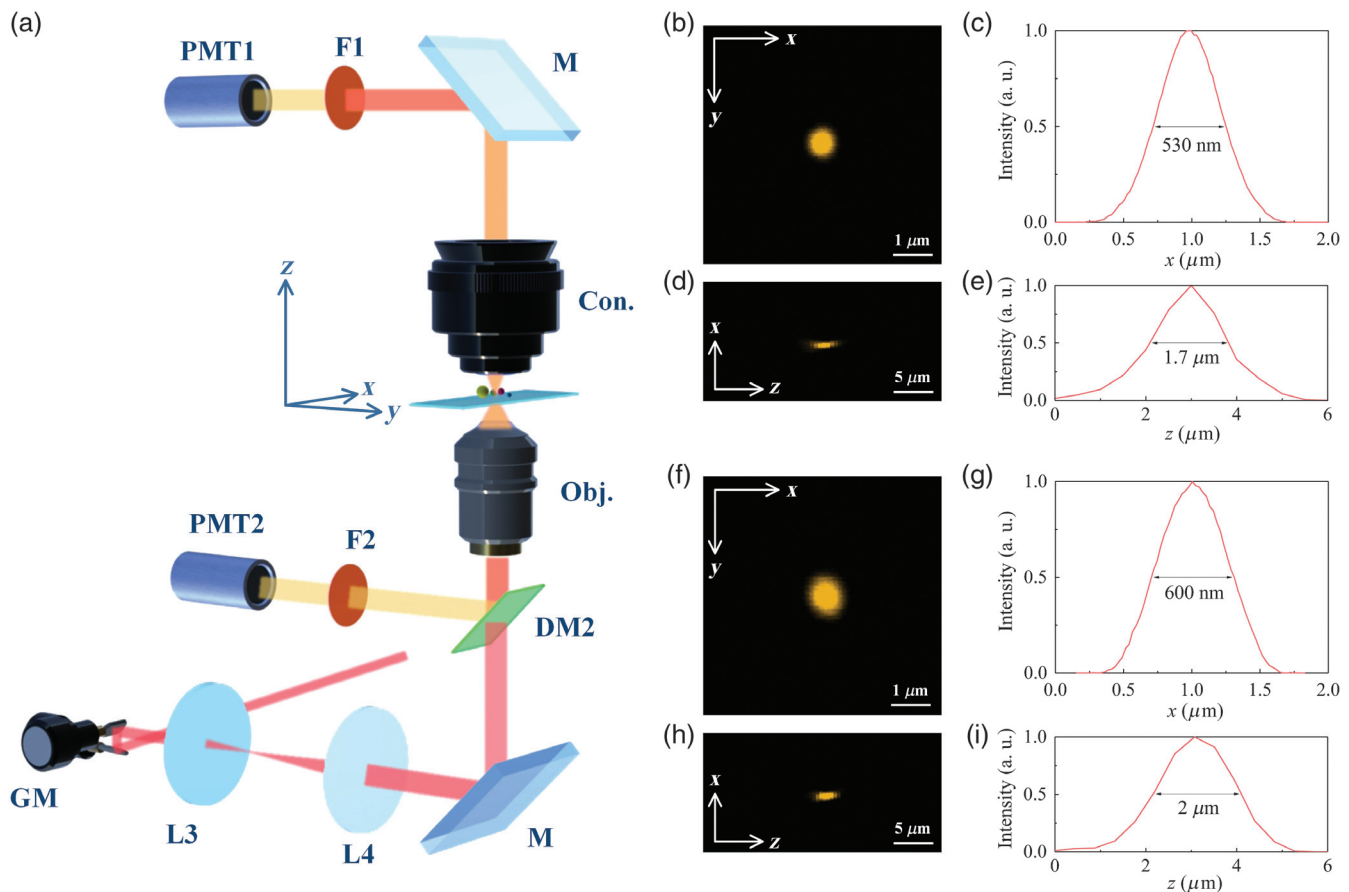
Fig. 4 (a) Schematic diagram of the 2PM experimental setup with both epi and transmitted detections. GM, galvanometric mirror; L, lens; M, mirror; Obj., objective; Con., condenser; DM, dichroic mirror; F, filters; PMT, photomultiplier tube. (b) Lateral and (d) axial PSFs of the transmitted-detection scheme. (c) The lateral resolution and (e) DOF of the transmitted-detection scheme. (f) Lateral and (h) axial PSFs of the epi-detection scheme. (g) The lateral resolution and (i) DOF of the epi-detection scheme. "a. u.": arbitrary units.

power increases. The reason is that the pulse width is being compressed when the signal propagates in the SMF, where the SMF provides the anomalous optical dispersion opposite to the NDF. The narrowing pulse width and increasing average power result in the soar of the peak power, which dramatically boosts the optical nonlinearity in the fiber. Owing to the SPM effect, the optical spectrum of the amplified signal is widely broadened, as shown in Fig. 3(e). The wavelength center is located at 1870 nm. The descend lines on the spectrum came from the absorption of water molecules in the air. The 3- and 5-dB bandwidths are 34 and 43 nm, respectively. The corresponding transform-limited sech^2 pulse width is 108 fs. The pulse width of the output beam was measured by an autocorrelator (*pulse*Check USB, APE). As shown in Fig. 3(f), the measured autocorrelation trace is well-fitted by the sech^2 function, and the pulse width is 133 fs. The slightly larger pulse width than the transform-limited calculation originates from the high-order dispersions. Based on the average power, repetition rate, and the pulse width of the output signal, the corresponding peak power is calculated to be ~285 kW after the amplifier.

The 937-nm laser was generated by frequency-doubling the 1.87-μm beam, and the obtained 937-nm power was ~60 mW. As the 1.87-μm after L1 was ~300 mW, the conversion efficiency was calculated to be 20%. The lateral beam profile is shown in Fig. 3(g), demonstrating a good Gaussian profile. The optical spectrum measured by the other OSA (AQ6370D, YOKOGAWA) is centered at 937 nm, and the 5-dB bandwidth is ~4 nm, as shown in Fig. 3(h). The side peaks in the frequency-doubled spectrum resulted from the low conversion efficiency of the long PPLN crystal. The pulse width was measured by the other autocorrelator (FR-103 MN, Femtochrome Research), illustrating a 353-fs pulse duration [Fig. 3(i)]. Further optimizing the crystal length will remove the side peaks and achieve a wider spectrum.[11] The frequency-doubled spectrum using a 1-mm-long PPLN crystal is shown in Fig. S2 in the Supplemental Material.

5 Experimental Setup of the 2PM

After building the laser source, a laser-scanning microscopy system was established for conducting the two-photon imaging. Figure 4(a) shows the experimental setup of the 2PM with detections of the epi-collected and transmitted fluorescence. A two-dimensional galvanometric mirror (GM, 6220H, Cambridge Technology) was used for laser scanning in the x-y plane. A telescope consisting of two lenses, L3 and L4, served to relay and expand the scanned laser to the back focal plane of the objective lens. Two objectives (60×, 1.2 NA,
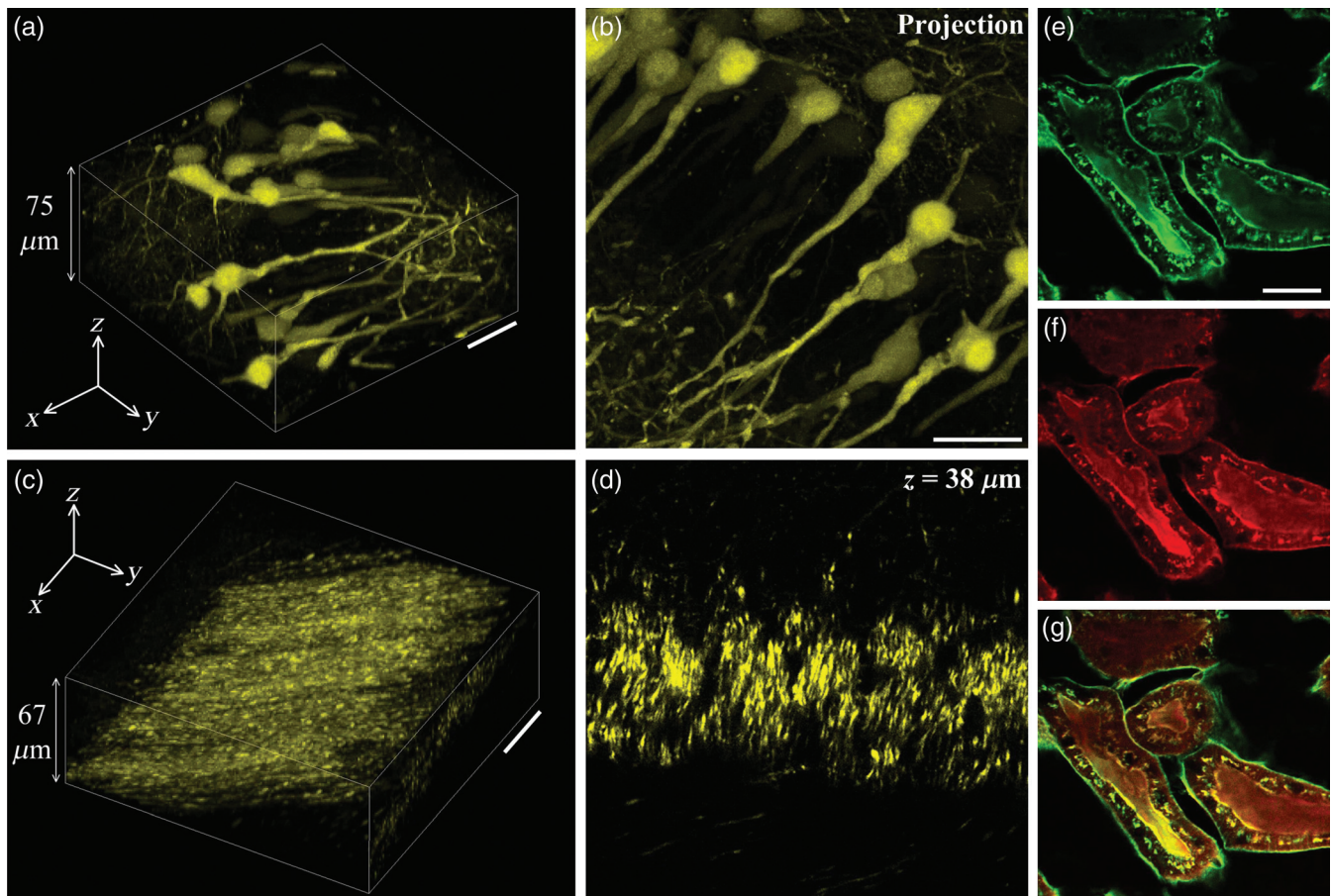
Fig. 5 (a)–(d) Two-photon fluorescence images of YFP-labeled neurons and fibers in a mouse brain slice. (e)–(g) Two-photon fluorescence images of Alexa Fluor 488- and Alexa Fluor 568-stained mouse kidney slice. Scale bar: 30 μm. FOV: 150 × 150 μm. Frame rate: 0.37 Hz (mouse brain) and 0.18 Hz (mouse kidney). Power after obj.: 18 mW (mouse brain) and 13 mW (mouse kidney).

UPlanSApo, Olympus; 25×, 1.05 NA, XLPLN25XWMP2, Olympus) were sequentially mounted in the 2PM for providing high resolution in transmitted detection and long working distance (2 mm) for imaging thick samples in the epi-detection, respectively. To match the back-aperture size of the objectives, for the 60× objective, L3 (focal length, $f_3 = 80$ mm) and L4 ($f_4 = 150$ mm) were used; for the 25× objective, L3 ($f_3 = 50$ mm) and L4 ($f_4 = 200$ mm) were utilized. The fluorescence signals generated were collected by the condenser in the transmitted path and the objective in the epi-path and detected by the photomultipliers PMT1 and PMT2 (H10723-20, Hamamatsu), respectively. DM2 (FF776, Semrock) was used to reflect the generated fluorescent signal to PMT2. The filters (F1 and F2, BSP01-785R, Semrock) were used to remove residual excitation light. The point spread function (PSF) was measured by imaging 200-nm fluorescent microspheres (F8809, Life Technologies Ltd.) for both epifluorescence and transmission channels. The microspheres were shifted along the z-axis with a step of 0.5 μm to obtain the axial PSFs. The lateral resolution of the transmitted detection channel is 530 nm, as shown in Figs. 4(b) and 4(c), while the corresponding depth of field (DOF) is 1.7 μm, as shown in Figs. 4(d) and 4(e). The lateral resolution and DOF for the epi-detection channel were 600 nm and 2 μm, respectively, as shown in Figs. 4(f)–4(i). The resolutions of both channels were thus sufficient for imaging cellular and subcellular fine structures. The transmission channel

(60×, obj.) was used to obtain Fig. 5, while the epi channel (25×, obj.) was used to obtain Figs. 6–8.

6 Imaging Results and Discussion

6.1 YFP-Labeled Mouse Brain Neuron and Alexa Fluor 488/568-Stained Mouse Kidney

We utilized the 937-nm laser to perform two-photon fluorescence imaging of a mouse brain slice in the transmitted channel. The sample was a 100-μm-thick Thy1-YFP mouse brain tissue sandwiched between two glass slides, where a subset of neuron expressed YFP. Layer-V pyramidal neurons in the prefrontal cortex were imaged in this paper. All experiments with these samples were approved and performed in accordance with institutional guidelines of the University of Hong Kong. Figure 5(a) shows a three-dimensional (3D) two-photon image of the neurons in the mouse brain within a thickness of 75 μm. The axial scanning step was 1 μm. The neuron distributions are clearly illustrated in the 3D reconstructed image. An axially projected view of the 3D image is shown in Fig. 5(b). The cell bodies and axons are well demonstrated. Figure 5(c) shows the dense fibers located at the external capsule of the mouse brain with a thickness of 67 μm. A typical lateral view of the fibers is shown in Fig. 5(d), which is located at the depth of 38 μm. The discriminations of adjacent small fibers indicate the good resolution of the 2PM.
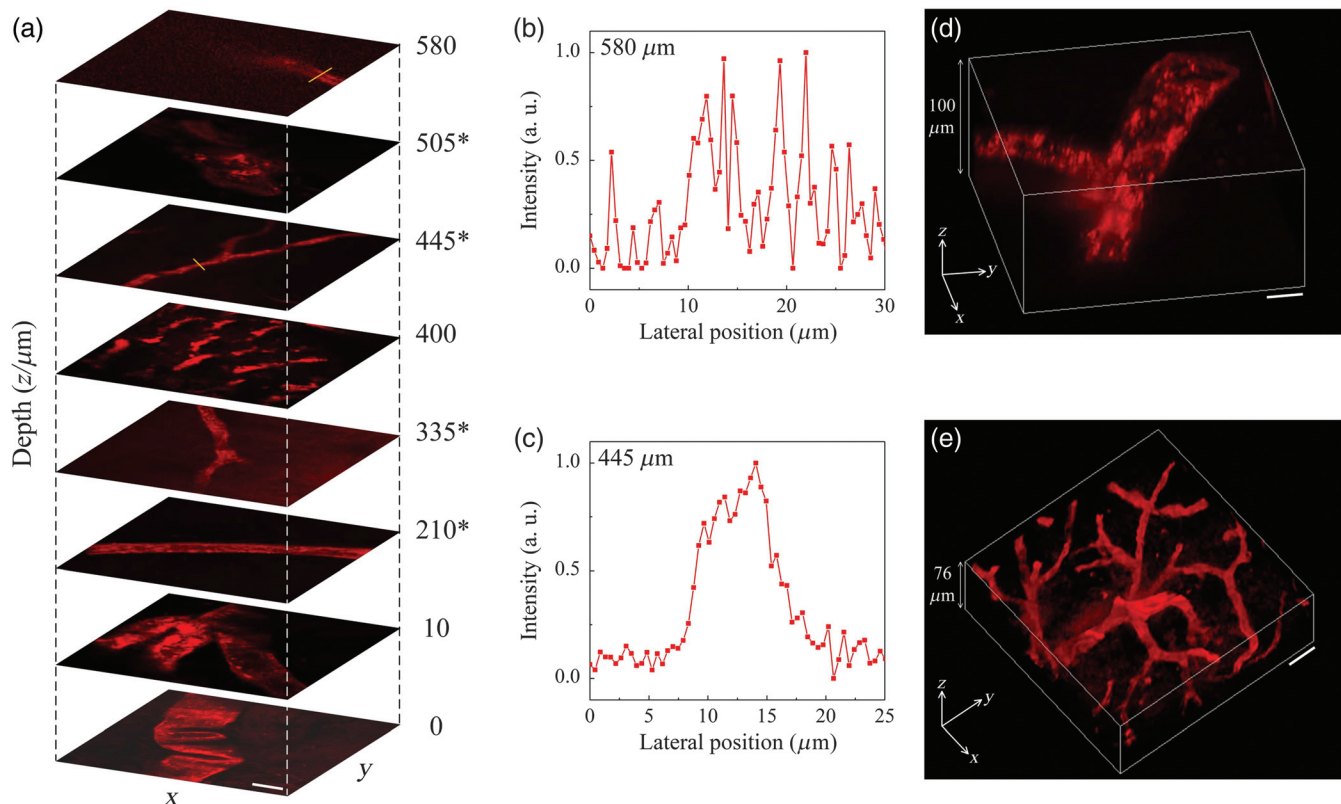
Fig. 6 (a) Two-photon fluorescence images of the DiI-stained vasculatures at different depths of the mouse brain. The depth value labeled with "*" denotes an axially projected image: 210*, 160 to 260 μm; 335*, 300 to 370 μm; 445*, 430 to 460 μm; 505*, 480 to 530 μm. The corresponding intensity profile of the blood vessel at the depth of (b) 580 μm and (c) 445 μm. "a. u.": arbitrary units. (d), (e) Vasculatures of different structures. Scale bar: 30 μm. FOV: 225 × 225 μm. Frame rate: 0.37 Hz. Power after obj.: 12 mW.

A mouse kidney slice (Thermo Fisher Scientific FluoCells® prepared slide #3) stained with multidyes was employed to demonstrate the two-color two-photon-excited fluorescence imaging. The sample is a 16-μm-thick cryosection stained with Alexa Fluor 488 wheat germ agglutinin (W-11261), Alexa Fluor 568 phalloidin (A-12380), and DAPI (D-1306). The two-photon excitation peaks of the Alexa Fluor 488 and Alexa Fluor 568 are 985 and 1028 nm, respectively, and are near the wavelength of our laser source, hence the two dyes can be excited simultaneously. While the two-photon excitation peak of the DAPI is ~685 nm, which is far away from the wavelength of the excitation laser, the DAPI-stained structures in the mouse kidney cannot be imaged by the 937-nm laser. Figures 5(e) and 5(f) show the Alexa Fluor 488-stained (green) and Alexa Fluor 568-stained (red) biostructures, which are achieved by isolating the emission of these two dyes with bandpass filters centered at 534 nm (FF01-534/42-25, Semrock) and 600 nm (FF01-600/52-25, Semrock), respectively. The composited image is shown in Fig. 5(g). It can be observed that the Alexa Fluor 488-stained glomeruli and convoluted tubules are highlighted in green, and the Alexa Fluor 568-stained filamentous actin prevalent in glomeruli and the brush border are also clear in red. The fluorescence intensity of the Alexa Fluor 568-stained structures is weaker than the Alexa Fluor 488, resulting from the lower excitation efficiency of the Alexa Fluor 568 by the 937-nm laser.

6.2 DiI-Stained Mouse Brain Vasculature

The 2PM was switched to the epi-detection mode for imaging the thick brain tissue. The sample is a mouse hemibrain with the endothelium labeled with the lipophilic tracer DiI (1, 1′-dioctadecyl-3,3,3′3′-tetramethylindocarbocyanine perchlorate) via transvascular perfusion. Figure 6(a) shows the images of the brain vasculatures located at different depths. As the vasculature structures extended beyond the field of view (FOV) of the objective during the axial scanning, the lateral position of the brain was slightly shifted to ensure the acquisitions of the vasculature images at different depths of the brain. High-resolution and contrast images of the blood vessels up to ~530 μm deep are capable of being achieved. The image contrast decreases when the imaging position goes deeper, as shown in the image of $z = 580$ μm, where the noise becomes serious. Figure 6(b) shows the corresponding intensity profile of a blood vessel. Its shape is hardly resolvable, and the background intensity is relatively high. As a comparison, the vessel profile at the depth of 445 μm demonstrates clear shapes, and the signal-to-background ratio (SBR) is also eminent, as shown in Fig. 6(c). The capacity of deep penetration results from the high peak power of the 937-nm laser owing to the low repetition rate, even though the two-photon excitation efficiency of the DiI dye at ~940 nm is ~3.3%.[33] Figures 6(d) and 6(e) show two typical 3D images of the blood vessels. The clear shapes and
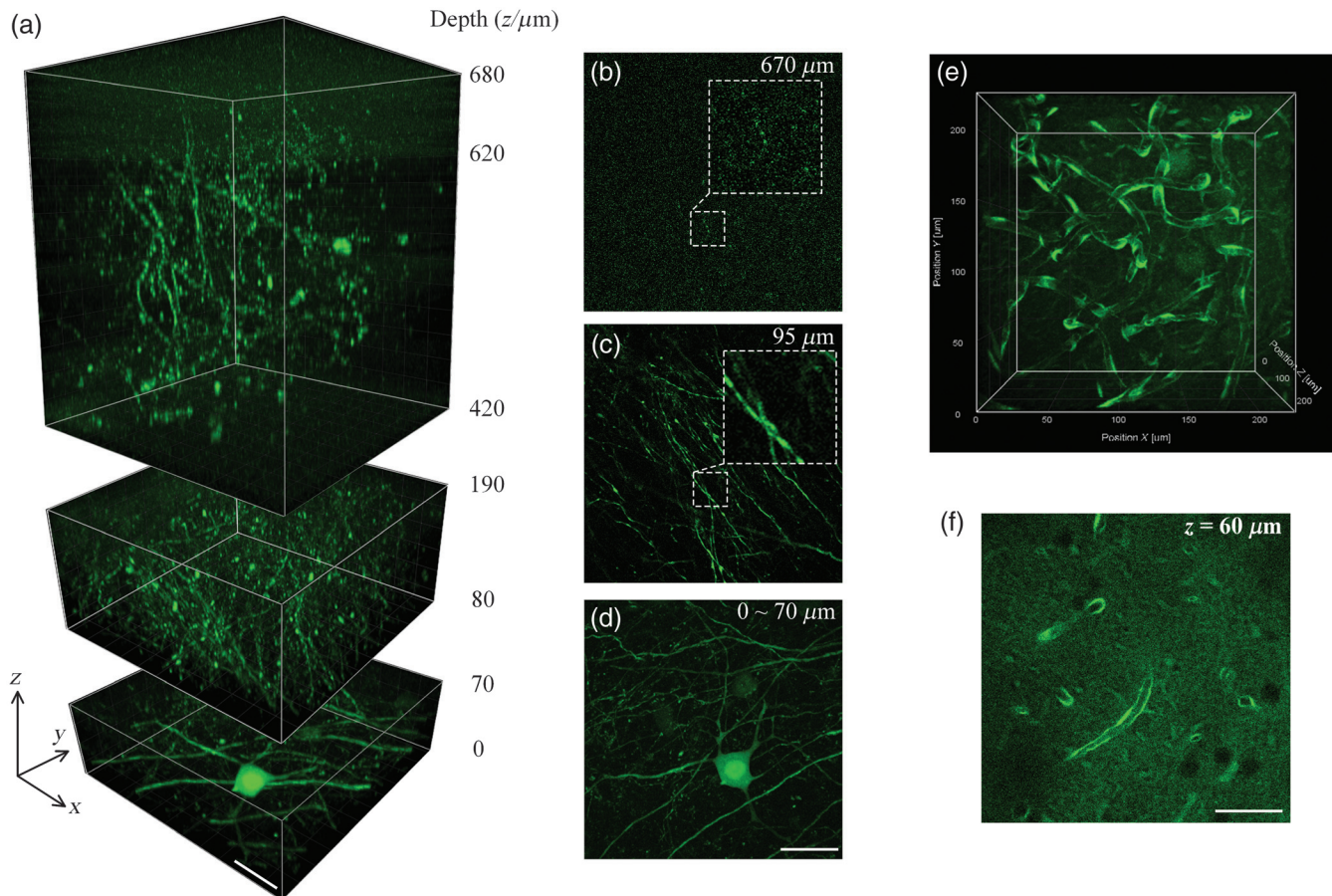
Fig. 7 (a) 3D reconstruction of the 2PM images of the EGFP-labeled mouse brain neurons. (b)–(d) Typical images of the neurons located at different depths. (e) 3D images of the GFP-labeled mouse brain vasculature. (f) Typical image of the blood vessel. Scalar bar: 50 μm.

distributions of the mouse brain vasculatures indicate the excellent power stability and high SNR of our excitation laser.

6.3 GFP-Labeled Neuron and Vasculature

We also performed the 2PM imaging of the GFP-labeled mouse brain neurons. The sample is a Thy1-GFP mouse hemibrain where a subset of layers III and V pyramidal expressed the fluorescent protein EGFP. The 3D reconstructed images are shown in Fig. 7(a). We scanned the brain up to the depth of 680 μm. The z-scan increments of the 0 to 70 and 80 to 190 μm depths are 1 μm, and, for the depth from 420 to 680 μm, it is 2 μm. The scanning speed for each frame is 2.7 s (512×512 pixels per frame). The average power after the objective at the surface (0 to 190 μm) of the brain was set to be $\sim$6 mW, and the power was increased to $\sim$10 mW when scanning deeper. The power after the objective is much lower than the 40-MHz fiber laser, which requires $\sim$200-mW power at the similar depth.[34] When the penetration is deeper than 620 μm, the SBR of the images is decreased owing to the light attenuation and scattering, as shown in Fig. 7(a). A typical image at the depth of 670 μm is shown in Fig. 7(b), where the background is serious. The cell body, axons, and fibers are well illustrated in the shallow positions of the brain, as shown in Figs. 7(c) and 7(d).

The GFP-labeled brain vasculatures were imaged within a thickness of 200 μm, as shown in Fig. 7(e), where the vascular system was well demonstrated. The sample is a transgenic rat brain slice that expresses GFP in endothelial cells. The GFP emits strong signals under the power of $\sim$10 mW. The frame time is 2.7 s, and the axial scan step is 2 μm. A typical image of the vasculature at the depth of 60 μm demonstrates the cross sections of blood vessels, as shown in Fig. 7(f).

6.4 SHG Imaging

SHG imaging was conducted in the epi-detection channel of the 2PM. A bandpass filter centered at 470 nm (bandwidth, 10 nm) was added before F2 to ensure only the SHG signal entered PMT2. A pair of half and quarter waveplates were put before the GM to control the polarization direction of the 937 nm laser on the samples. The samples were obtained from a wild-type C57BL/6 mouse after transcardial perfusion fixation using 4% paraformaldehyde. Figure 8 shows the SHG images of the fibrillar collagens in multiple regions of the mouse skull, leg muscle, and tail tendon, demonstrating the robustness and versatility of our laser source for random imaging positions. The beam polarization was adjusted to let the tissue structures in the FOV emit the maximum intensity. Although the epi-detection would have resulted in decreased signal intensity because less SHG signal is produced by backscattering, the collagen fibers in the tissues can still be easily detected under a low illumination power, which is attributed to the efficient excitation by the low-repetition-rate laser.

7 Conclusions

We have demonstrated a $\sim$9-MHz, 133-fs, and 38-nJ all-fiber mode-locked laser at 1.8 μm for frequency doubling to 937 nm utilized in the 2PM. The 1.8-μm laser is mode-locked by controlling the ASE spectrum of the TDF instead of using wavelength-selecting components and utilizes a single-stage amplification to simultaneously boost the power and compress the pulse width, realizing a compact footprint ($30 \times 30 \times 5$ cm^3) and self-starting regime. Compared with the frequency-shifted laser source, the directly mode-locked laser has a high SNR of 74 dB, which is beneficial to providing clean backgrounds for two-photon images. The 937-nm laser is suitable for versatile biological tissues and fluorescence dyes in the 2PM, including the GFP/YFP-labeled mouse brain neurons, DiI-stained and GFP-labeled blood vessels, Alexa Fluor 488/568-stained mouse kidney, and SHG imaging of the intact mouse skull, leg, and tail. Benefiting from the low repetition rate and high SNR of the excitation laser, the penetration depth in mouse brain tissues is up to 620 μm with an illumination power as low as $\sim$10 mW, much lower than the 40-MHz fiber laser, which requires $\sim$200-mW power at the similar depth.[34] Even for the DiI dye with an extremely low excitation efficiency of 3.3%, the penetration depth is still up to 530 μm, indicating that the low-repetition-rate source works efficiently for a wide range of dyes with a fixed excitation wavelength. The low-repetition-rate and high-SNR excitation source at 937 nm with compact size and low cost holds great potential for biological investigations, such as *in vivo* deep-tissue imaging.
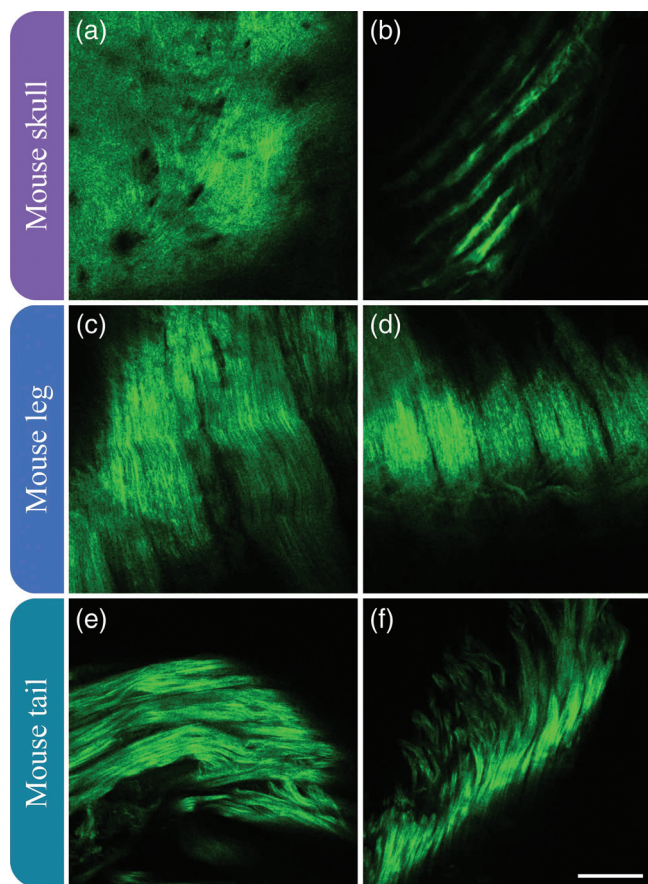
Fig. 8 SHG images of the mouse [(a), (b)] skull, [(c), (d)] leg, and [(e), (f)] tail. FOV: 225×225 μm. Frame rate: 0.19 Hz. Power after obj.: 10 mW. Scale bar: 50 μm.

Technology Commission of the Hong Kong SAR Government. The authors declare no conflicts of interest.

Data availability

References

1. F. Helmchen and W. Denk, "Deep tissue two-photon microscopy," *Nat. Methods* **2**, 932–940 (2005).
2. J. Wu, N. Ji, and K. K. Tsia, "Speed scaling in multiphoton fluorescence microscopy," *Nat. Methods* **15**, 800–812 (2021).
3. W. Zong et al., "Fast high-resolution miniature two-photon microscopy for brain imaging in freely behaving mice," *Nat. Methods* **14**, 713–719 (2017).
4. J. Wu et al., "Kilohertz two-photon fluorescence microscopy imaging of neural activity *in vivo*," *Nat. Methods* **17**, 287–290 (2020).
5. N. Ji, J. C. Magee, and E. Betzig, "High-speed, low-photodamage nonlinear imaging using passive pulse splitters," *Nat. Methods* **5**, 197–202 (2008).
6. R. Hoebe et al., "Controlled light-exposure microscopy reduces photobleaching and phototoxicity in fluorescence live-cell imaging," *Nat. Biotechnol.* **25**, 249–253 (2007).
7. J. Icha et al., "Phototoxicity in live fluorescence microscopy, and how to avoid it," *BioEssays* **39**, 1700003 (2017).
8. G. Donnert, C. Eggeling, and S. W. Hell, "Major signal increase in fluorescence microscopy through dark-state relaxation," *Nat. Methods* **4**, 81–86 (2007).
9. X. Gao et al., "Core-pumped femtosecond Nd:fiber laser at 910 and 935 nm," *Opt. Lett.* **39**, 4404–4407 (2014).
10. B. Chen et al., "910 nm femtosecond Nd-doped fiber laser for *in vivo* two-photon microscopic imaging," *Opt. Express* **24**, 16544–16549 (2016).
11. C.-H. Hage et al., "Two-photon microscopy with a frequency-doubled fully fusion-spliced fiber laser at 1840 nm," *Opt. Lett.* **43**, 5098–5101 (2018).
12. R. Dai et al., "High energy (>40 nJ), sub-100 fs, 950 nm laser for two-photon microscopy," *Opt. Express* **29**, 38979–38988 (2021).
13. J. W. Dawson et al., "High-power 938-nm cladding pumped fiber laser," *Proc. SPIE* **4974**, 75–82 (2003).
14. S. Fu et al., "High-efficiency Nd^{3+}-doped phosphate fiber laser at 880 nm," *IEEE Photonics Technol. Lett.* **32**, 1179–1182 (2020).
15. K. Arai et al., "Aluminum or phosphorus co-doping effects on the fluorescence and structural properties of neodymium-doped silica glass," *J. Appl. Phys.* **59**, 3430–3436 (1986).
16. K. Qian et al., "Mode-locked Nd-doped fiber laser at 930 nm," *Opt. Lett.* **39**, 267–270 (2014).
17. A. Wang, A. George, and J. Knight, "Three-level neodymium fiber laser incorporating photonic bandgap fiber," *Opt. Lett.* **31**, 1388–1390 (2006).
18. B. Chen et al., "Robust hollow-fiber-pigtailed 930 nm femtosecond Nd:fiber laser for volumetric two-photon imaging," *Opt. Express* **25**, 22704–22709 (2017).
19. W. Liu et al., "Self-phase modulation enabled, wavelength-tunable ultrafast fiber laser sources: an energy scalable approach," *Opt. Express* **24**, 15328–15340 (2016).
20. P. Wang et al., "926 nm Yb-doped fiber femtosecond laser system for two-photon microscopy," *Appl. Phys. Express* **12**, 032008 (2019).
21. K. Charan et al., "Fiber-based tunable repetition rate source for deep tissue two-photon fluorescence microscopy," *Biomed. Opt. Express* **9**, 2304–2311 (2018).
22. N. G. Horton et al., "*In vivo* three-photon microscopy of subcortical structures within an intact mouse brain," *Nat. Methods* **7**, 205–209 (2013).
23. A. Zach et al., "All-fiber widely tunable ultrafast laser source for multimodal imaging in nonlinear microscopy," *Opt. Lett.* **44**, 5218–5221 (2019).
24. B. Li et al., "Investigation of the long wavelength limit of soliton self-frequency shift in a silica fiber," *Opt. Express* **26**, 19637–19647 (2018).
25. J. M. Dudley, G. Genty, and S. Coen, "Supercontinuum generation in photonic crystal fiber," *Rev. Mod. Phys.* **78**, 1135 (2006).
26. C. Xu and W. W. Webb, "Measurement of two-photon excitation cross sections of molecular fluorophores with data from 690 to 1050 nm," *J. Opt. Soc. Am. B-Opt. Phys.* **13**, 481–491 (1996).
27. Y. Hontani, F. Xia, and C. Xu, "Multicolor three-photon fluorescence imaging with single-wavelength excitation deep in mouse brain," *Sci. Adv.* **7**, eabf3531 (2021).
28. FPbase, "EGFP," https://www.fpbase.org/protein/egfp/.
29. FPbase, "EYFP," https://www.fpbase.org/protein/eyfp/.
30. P. Ciąćka et al., "Dispersion measurement of ultra-high numerical aperture fibers covering thulium, holmium, and erbium emission wavelengths," *J. Opt. Soc. Am. B-Opt. Phys.* **35**, 1301–1307 (2018).
31. D. Strickland and G. Mourou, "Compression of amplified chirped optical pulses," *Opt. Commun.* **55**, 447–449 (1985).
32. C. Li et al., "Fiber chirped pulse amplification of a short wavelength mode-locked thulium-doped fiber laser," *APL Phontonics* **2**, 121302 (2017).
33. University of Arizona, "Spectra Database," http://spectra.arizona.edu/.
34. E. P. Perillo et al., "Deep *in vivo* two-photon microscopy with a low cost custom built mode-locked 1060 nm fiber laser," *Biomed. Opt. Express* **7**, 324–334 (2016).
35. K. Takasaki, R. Abbasi-Asl, and J. Waters, "Superficial bound of the depth limit of two-photon imaging in mouse brain," *eNeuro* **7**, ENEURO.0255-19.2019 (2020).
36. A. Birkner, C. H. Tischbirek, and A. Konnerth, "Improved deep two-photon calcium imaging *in vivo*," *Cell Calcium* **64**, 29–35 (2017).

Biographies of the authors are not available.